

Modeling Large Air Fraction Holey Optical Fibers

Tanya M. Monro, D. J. Richardson, N. G. R. Broderick, and P. J. Bennett

Abstract—We develop a modal decomposition approach to solve the full vector wave equation for holey optical fibers (HF). This model can be used to explore the modal properties of a wide range of HF's, including those with large air holes. The optical properties of HF can be tailored via the arrangement of the air holes, and this flexibility leads to a wide range of practical applications.

Index Terms—Eigenfunctions, eigenvalues, modeling, optical dispersion, optical fiber applications, orthogonal function methods, periodic structures.

I. INTRODUCTION

THE flexibility offered by holey optical fibers has generated a great deal of interest in these rather unusual structures. The cladding region in a holey fiber (HF) consists of a large number of air holes running along the length of the fiber. Fig. 1 is an SEM photograph of a typical HF structure. HF's guide light due to the effective refractive index difference between the core (formed by the absence of an air hole—see Fig. 1) and the cladding.

For some specific periodic arrangements of the air holes, a bandgap forms in the transverse plane, [1] and then the absence of a single hole creates a localized state within the bandgap which can be used to guide light along with fiber. Such fibers are usually referred to as photonic crystal fibers (PCF's), and we do not explicitly consider this guidance mechanism here. Instead we investigate a broader range of fiber structures; in a HF, the holes do not need to conform to a periodic distribution in order to guide light. HF's exhibit unique transmission characteristics (see [2] and [3]), and many of these properties can be tailored via the hole distribution.

Most of the unusual properties of HF arise from the fact that the effective index difference between core and cladding is a strong function of wavelength, since at longer wavelengths the modal field extends further into the air holes thereby reducing the effective cladding index. As a consequence, some HF's can be single-moded regardless of the wavelength [2]. Another result of the HF geometry is that a significant fraction of the modal power can be located inside the holes, which suggests that these fibers may be useful as evanescent field devices [5], [6].

The first model developed for HF's was the *effective index model* [2], which uses an equivalent step-index fiber approximation. Although this model provides some useful analytical results, it cannot accurately predict properties such as dispersion or birefringence. These quantities depend critically on the geometry, and this approach ignores the complex transverse index

profile in HF. In the full-vector technique described by Ferrando *et al.* [7], the modal fields and the refractive index profile are decomposed into plane wave components, and by doing this the wave equation is reduced to an eigenvalue problem. Although this approach can account for the complicated cladding structure of HF, it is computationally intensive. Also, the refractive index profile is defined over a restricted region, and periodic boundary conditions are used to extend the structure spatially. This imposes an additional periodicity on the system which is somewhat restrictive for HF's, which, unlike PCF's, do not need to be periodic.

Alternative scalar approaches were developed independently by Mogilevtsev *et al.* [8] and ourselves [3], and in both approaches the electric field was described using localized Hermite–Gaussian functions. This is efficient because it takes advantage of the localization of the guided modes. However, this approach cannot be accurate unless the refractive index is also represented well. Reference [8] does not describe the way in which they chose to describe the index distribution, but in our method the central index defect and the air hole lattice are described independently. We decompose the electric field and index defect using localized functions, and the lattice of air holes using periodic functions. This approach is efficient because the quantities are decomposed using functions chosen carefully to suit, and so a small number of terms can be used. Also, like the purely plane-wave approach, this model can accurately describe the complex transverse structures found in HF.

To accurately model HF's with large air holes, it is crucial to use a full vector model. In [3] we found that when $d/\Lambda > 0.35$ the scalar approximation becomes inadequate (see Fig. 2 for definitions of d and Λ). In particular, it is crucial to use a vector model when predicting sensitive quantities such as dispersion. Here we extend the scalar model from [3] to a full vector model of light propagation to enable us to accurately predict the properties of a much fuller range of HF's.

II. FULL MODAL VECTOR MODEL

A. Background

As we are exploring the modal properties of HF, we take the fiber to be uniform in the propagation (z) direction, and so the modal electric field can be written in the form

$$E_j(x, y, z) = (e_j^t(x, y) + e_j^z(x, y)\hat{z}) \exp(i\beta_j z) \quad (1)$$

where β_j is the propagation constant of the j th mode, and e_j^t and e_j^z are the transverse and longitudinal components of the modal electric field respectively. The axes used here are defined in Fig. 2.

Manuscript received April 16, 1999. This work was supported in part by EPSRC Grant GR/L31388 and the Royal Society University Fellowship.

The authors are with the Optoelectronics Research Center, University of Southampton, Southampton SO17 1BJ, U.K. (e-mail: tmm@orc.soton.ac.uk).

Publisher Item Identifier S 0733-8724(00)00390-X.

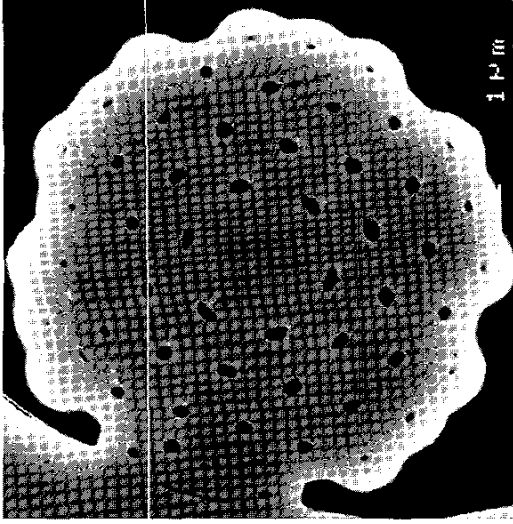


Fig. 1. SEM photograph of a holey fiber cross-section, $d/\Lambda \approx 0.2$ (where d is the hole diameter, Λ the hole separation). In this fiber the HF structure has been enclosed in a solid jacket (see bottom left) to reduce its fragility.

We start by writing the transverse component of the modal electric field in the following general form:

$$\mathbf{e}_j^t = e_x \hat{\mathbf{x}} + e_y \hat{\mathbf{y}}. \quad (2)$$

Using (1) and (2) in the full vector wave equation, we obtain the following pair of coupled equations for the electric field components $e_x(x, y)$ and $e_y(x, y)$ [9]

$$\begin{cases} \left[\frac{\nabla^2}{k^2} - \frac{\beta^2}{k^2} + n^2 \right] e_x = \frac{-1}{k^2} \frac{\partial}{\partial x} \left(e_x \frac{\partial \ln n^2}{\partial x} + e_y \frac{\partial \ln n^2}{\partial y} \right) \\ \left[\frac{\nabla^2}{k^2} - \frac{\beta^2}{k^2} + n^2 \right] e_y = \frac{-1}{k^2} \frac{\partial}{\partial y} \left(e_x \frac{\partial \ln n^2}{\partial x} + e_y \frac{\partial \ln n^2}{\partial y} \right) \end{cases} \quad (3)$$

where $k = 2\pi/\lambda$ is the wavenumber and $n = n(x, y)$ is the transverse refractive index profile. The subscript labeling the mode number (j) has been dropped for brevity.

To solve (3) for HF's, we decompose the transverse refractive index profile and the modal electric field using orthogonal functions. The choice of functions is crucial in making this method efficient and accurate, and they are described briefly in Section II-B.

B. Decompositions

The modal electric field is expanded as

$$\mathbf{e}^t(x, y) = \sum_{a,b=0}^{F-1} (\mathcal{E}_{ab}^x \psi_a^m(x) \psi_b^m(y) \hat{\mathbf{x}} + \mathcal{E}_{ab}^y \psi_a^m(x) \psi_b^m(y) \hat{\mathbf{y}}) \quad (4)$$

[see (2)] where the ψ_a^m are orthonormal Hermite–Gaussian functions with a characteristic width $w_m \propto \Lambda$, where Λ is the interhole separation. More details are given in [3]. Using this decomposition, only a few terms are needed to reconstruct observed modal profiles.

The transverse refractive index profile is described in two parts. The periodic lattice of holes is described using periodic

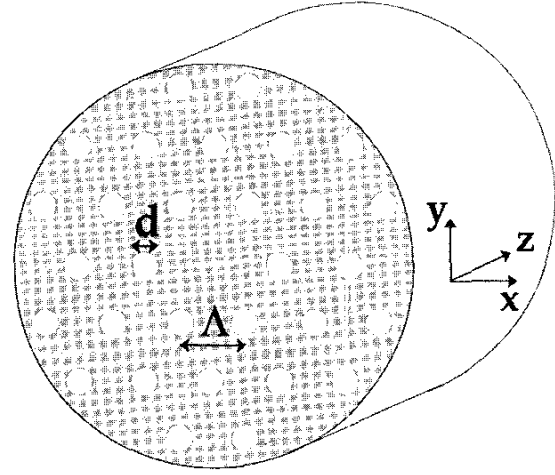


Fig. 2. Idealized HF cross-section.

functions, and the central index defect is described using Hermite–Gaussians of characteristic width $w_d \propto d$, where d is the defect diameter, as then fewer terms are required for accuracy. Hence, we write

$$n^2 = \sum_{a,b=0}^{C-1} c_{ab} \mathcal{C}(x, y) + \sum_{a,b=0}^{P-1} P_{ab} \mathcal{P}(x, y) \quad (5)$$

where \mathcal{C} and \mathcal{P} terms are used for the defect and holes, respectively, and

$$\mathcal{C}(x, y) = \psi_a^d(x) \psi_b^d(y) \quad (6)$$

$$\mathcal{P}(x, y) = \cos\left(\frac{2a\pi x}{\ell}\right) \cos\left(\frac{2b\pi y}{\ell}\right) \quad (7)$$

ℓ is the transverse extent of the structure, and ψ_a^d is ψ_a^m with w_m replaced by w_d .

To avoid producing overlap integrals which cannot be evaluated analytically, we choose also to expand $\ln(n^2)$ using the same functions [see (3)]. Hence we write

$$\ln(n^2) = \sum_{a,b=0}^{C-1} c_{ab}^{\ln} \mathcal{C}(x, y) + \sum_{a,b=0}^{P-1} p_{ab}^{\ln} \mathcal{P}(x, y). \quad (8)$$

This decomposition makes the calculation significantly more efficient, and it is natural to use the same functions to decompose $\ln(n^2)$, as it has the same spatial feature distribution as n^2 . For a given HF, the coefficients c_{ab} , c_{ab}^{\ln} , p_{ab} , and p_{ab}^{\ln} are evaluated by performing overlap integrals, and they only need to be calculated once for any structure.

C. Electric Field Polarization

The decompositions defined in Section II-B can be used to turn (3) into an eigenvalue problem, and this procedure is described in [3] for the scalar case. For HF's of the type shown in Figs. 1 and 2, the modal field and the index profile are both symmetric, which is why the even basis set given in Section II-B can be used to represent them. When these decompositions are used in the vector wave equation the equations for the x - and y -components of the field (3) decouple.

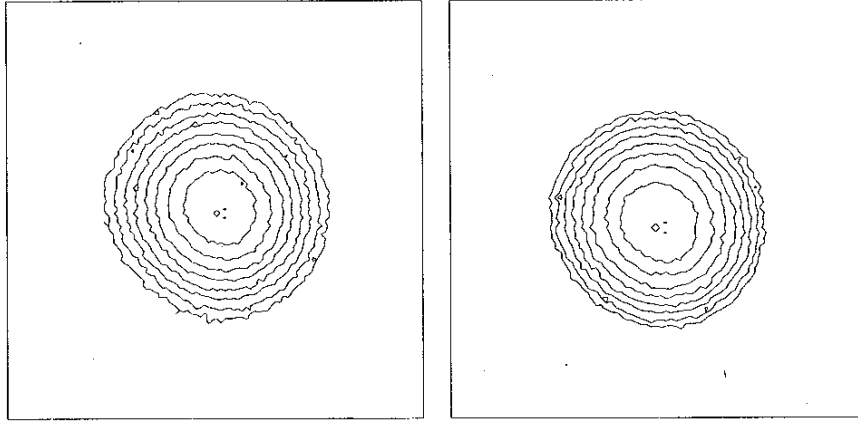


Fig. 3. Left, mode of the HF from Fig. 1 when polarizers were aligned for maximum throughput. Right, the polarizer at the output was rotated by 90° . The gain was adjusted for the second image (at least 30 dB extinction occurs over 90°), and the contour levels are separated by 0.5 dB. Note that there is no significant change in the shape of the mode.

The fact that (3) decouple is important, because it implies that the modes of HF's must be linearly polarized. This has been confirmed experimentally using a length of the HF shown in Fig. 1. Light at $1.5 \mu\text{m}$ was launched into the fiber, and plane polarizers were inserted at both the output and input ends. The left plot in Fig. 3 shows the fundamental mode from this fiber when the polarizers were aligned to give maximum power throughput. As the polarizer at the output was rotated, we found that mode intensity decreased until at 90° rotation it was extinguished by at least 30 dB. The plot on the right in Fig. 3 shows the mode after the 90° rotation; the camera gain has been adjusted so that the mode shapes can be compared more easily. Notice that no significant distortion of the mode shape occurs during this rotation. This experiment was done for different orientations of the polarizer at the input end, and the result was unchanged.

The fact that the mode is extinguished by the rotation of the output polarizer without any distortion of the mode shape leads us to conclude that to a good approximation, the fundamental modes are linearly polarized in this fiber. We expect that this will remain true for other HF's with similar symmetry properties.

In order to model HF with an asymmetric index profile or to obtain accurate predictions for the second-mode cutoff, it is necessary to use both odd and even basis functions in the decompositions. Then the x - and y -components of the wave equation would no longer decouple. Although only even basis functions are used here for simplicity, it is straightforward to add odd functions to our decompositions, and we expect that this approach should remain accurate and efficient with this extension.

D. Eigenvalue System

As described in Section II-C, for the structures considered here, the vector wave equations for the x - and y -components of the modal field separate, and so they can be considered independently. We assign the x and y polarizations the propagation constants β_x and β_y , respectively.

Using the decompositions described in Section II-B, the vector wave equations then reduce to the following eigenvalue systems:

$$\begin{aligned} M_x \hat{v}_x &= \frac{\beta_x^2}{k^2} \hat{v}_x \\ M_y \hat{v}_y &= \frac{\beta_y^2}{k^2} \hat{v}_y \end{aligned} \quad (9)$$

where the eigenvectors \hat{v}_α have components defined by the modal field coefficients thus: $(\mathcal{E}_{00}^\alpha \dots \mathcal{E}_{0F}^\alpha \quad \mathcal{E}_{10}^\alpha \dots \mathcal{E}_{FF}^\alpha)$ where $F - 1$ has been replaced by F for compactness, and $\alpha = x, y$. The matrices M_α from (9) take the form

$$\begin{pmatrix} \mathcal{M}_{0000}^\alpha & \dots & \mathcal{M}_{000F}^\alpha & \mathcal{M}_{0010}^\alpha & \dots & \mathcal{M}_{00FF}^\alpha \\ \vdots & \vdots & \vdots & \vdots & \vdots & \vdots \\ \mathcal{M}_{0F00}^\alpha & \dots & \mathcal{M}_{0F0F}^\alpha & \mathcal{M}_{0F10}^\alpha & \dots & \mathcal{M}_{0FFF}^\alpha \\ \mathcal{M}_{1000}^\alpha & \dots & \mathcal{M}_{100F}^\alpha & \mathcal{M}_{1010}^\alpha & \dots & \mathcal{M}_{10FF}^\alpha \\ \vdots & \vdots & \vdots & \vdots & \vdots & \vdots \\ \mathcal{M}_{FF00}^\alpha & \dots & \mathcal{M}_{FF0F}^\alpha & \mathcal{M}_{FF10}^\alpha & \dots & \mathcal{M}_{FFFF}^\alpha \end{pmatrix} \quad (10)$$

where

$$\mathcal{M}_{abcd}^\alpha = \frac{1}{k^2} I_{abcd}^{(1)} + I_{abcd}^{(2)} + \frac{1}{k^2} I_{abcd}^{(3), \alpha} \quad (11)$$

and the I are overlap integrals of the modal functions, defined as

$$\begin{aligned} I_{abcd}^{(1)} &= \int_{-\infty}^{\infty} \int_{-\infty}^{\infty} \psi_a^m(x) \psi_b^m(y) \nabla^2 [\psi_c^m(x) \psi_d^m(y)] dx dy \\ I_{abcd}^{(2)} &= \int_{-\infty}^{\infty} \int_{-\infty}^{\infty} n^2 \psi_a^m(x) \psi_b^m(y) \psi_c^m(x) \psi_d^m(y) dx dy \\ I_{abcd}^{(3), \alpha} &= \int_{-\infty}^{\infty} \int_{-\infty}^{\infty} \psi_a^m(x) \psi_b^m(y) \\ &\quad \times \frac{\partial}{\partial \alpha} \left(\psi_c^m(x) \psi_d^m(y) \frac{\partial [\ln(n^2)]}{\partial \alpha} \right) dx dy. \end{aligned} \quad (12)$$

It is straightforward to evaluate $I^{(1)}$ analytically, and $I^{(2)}$ and $I^{(3)}$ simplify to

$$\begin{aligned}
 I_{abcd}^{(2)} &= \sum_{f,g=0}^{C-1} c_{fg} I_{fac}^{(22)} I_{gbd}^{(22)} + \sum_{f,g=0}^{P-1} p_{fg} I_{fac}^{(21)} I_{gbd}^{(21)} \\
 I_{abcd}^{(3),x} &= - \sum_{f,g=0}^{C-1} c_{fg}^{\ln} I_{gbd}^{(22)} I_{fac}^{(31)} - \sum_{f,g=0}^{P-1} p_{fg}^{\ln} I_{gbd}^{(21)} I_{fac}^{(32)} \\
 I_{abcd}^{(3),y} &= - \sum_{f,g=0}^{C-1} c_{fg}^{\ln} I_{fac}^{(22)} I_{gbd}^{(31)} - \sum_{f,g=0}^{P-1} p_{fg}^{\ln} I_{fac}^{(21)} I_{gbd}^{(32)} \quad (13)
 \end{aligned}$$

where

$$\begin{aligned}
 I_{i_1 i_2 i_3}^{(21)} &= \int_{-\infty}^{\infty} \cos\left(\frac{2i_1 \pi s}{\ell}\right) \psi_{i_2}^m(s) \psi_{i_3}^m(s) ds \\
 I_{i_1 i_2 i_3}^{(22)} &= \int_{-\infty}^{\infty} \psi_{i_1}^d(s) \psi_{i_2}^m(s) \psi_{i_3}^m(s) ds \\
 I_{i_1 i_2 i_3}^{(31)} &= \int_{-\infty}^{\infty} \frac{\partial \psi_{i_1}^m(s)}{\partial s} \psi_{i_2}^m(s) \frac{\partial \psi_{i_3}^m(s)}{\partial s} ds \\
 I_{i_1 i_2 i_3}^{(32)} &= \int_{-\infty}^{\infty} \frac{\partial \psi_{i_1}^m(s)}{\partial s} \psi_{i_2}^m(s) \frac{\partial \phi_{i_3}(s)}{\partial s} ds \quad (14)
 \end{aligned}$$

and s is simply a dummy variable of integration. The overlap integrals in (14) can be evaluated analytically for the decompositions chosen in Section II-B, even though the mode and index defect have different characteristic widths ($w_m \neq w_d$). This is a significant advantage, as numerical calculation of these overlaps is computationally intensive.

By solving (9) the modes and corresponding propagation constants of the fiber can be calculated. For this full vector problem, a guided mode consists of a polarization doublet formed by x - and y -components of the mode, and each component has an associated propagation constant. Both M_x and M_y are $F^2 \times F^2$ matrices, and so the solution to each eigenvalue equation produces F^2 eigenvalue/eigenvector pairs. Only one or at most a few of these pairs correspond to guided modes of the fiber, and these modes can be distinguished by extracting the eigenvalues (β_z^2/k^2) which fall within the range allowed by the structure (see [3]).

III. RESULTS

Using the full vector model presented in Section II, a much wider range of holey fibers (HF's) can be explored. In particular, it gives us the flexibility to probe HF's with large air fractions, and we find that these fibers have a rich and diverse range of properties.

A. A Typical HF

We begin by presenting some results of our vector method for a typical large air fraction HF. Fig. 4 shows an SEM image of a HF we have fabricated with a relative hole size of $d/\Lambda \approx 0.6$ and a hole spacing of $\Lambda = 3.2 \mu\text{m}$. Note that unlike the fiber shown in Fig. 1, the air holes in this fiber are large enough that the full vector model is required. Here we describe the model

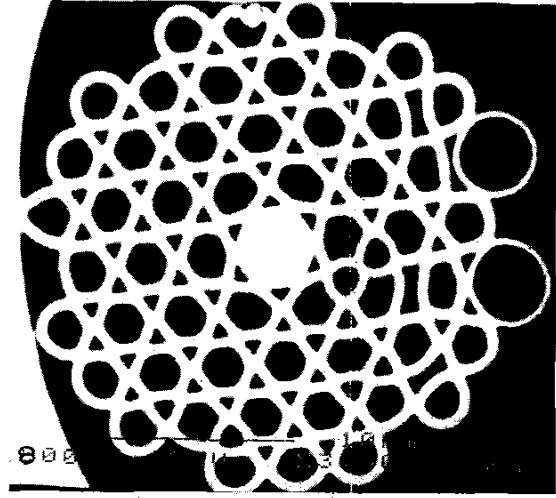


Fig. 4. SEM of a holey fiber with $d/\Lambda \approx 0.6$. Again, the structure was enclosed in a solid jacket to reduce its fragility.

predictions, beginning with the simplest approximation for this HF structure.

1) *The First Approximation:* We begin by describing some results of the vector model for a HF with a perfect hexagonal arrangement of holes. We use the parameters of the fiber in Fig. 4: a relative hole size of $d/\Lambda = 0.6$ and an interhole separation of $\Lambda = 3.2 \mu\text{m}$. This is clearly a simplification because we assume that the holes lie on a regular hexagonal lattice, and we ignore the small interstitial air holes between the large air holes in Fig. 4. These extra holes are typically only found in large air fraction HF; in small air fraction HF the interstitials normally close up during fabrication. Section III-A2 investigates the effect interstitial holes can have on the modal properties of HF.

Fig. 5 shows the intensity profiles of the fundamental modes at $\lambda = 1.5 \mu\text{m}$ for this HF as calculated using the new vector model when $P = 100$, $C = F = 10$ terms are used. The refractive index profile is superimposed on the modal profiles, and the left and right plots show the x - and y -components of the polarization doublet respectively. Both components of the fundamental mode reflect the hexagonal lattice symmetry. Slight differences between these components are apparent; for example the x -component is somewhat more extended in the x (horizontal) direction. Although these modes are similar, this does not imply that it is valid to ignore the vector terms in the wave equation.

The full vector model predicts that the area A_{eff} (see Section III-B for definition) of the fundamental mode of this HF is approximately $12 \mu\text{m}^2$ for both the x - and y -components. This is a relatively small mode area when compared with more conventional fibers, and could be useful in enhancing nonlinear effects in these fibers. However, often a large mode area is desired in order that nonlinear effects can be avoided altogether, and in Section III-B we discuss the ways in which the mode area in a HF can be tailored.

When a HF has large air holes, the effective index difference between the core and the cladding is a very strong function of wavelength, and hence this type of fiber is highly dispersive. The group velocity dispersion (GVD) of the HF described above

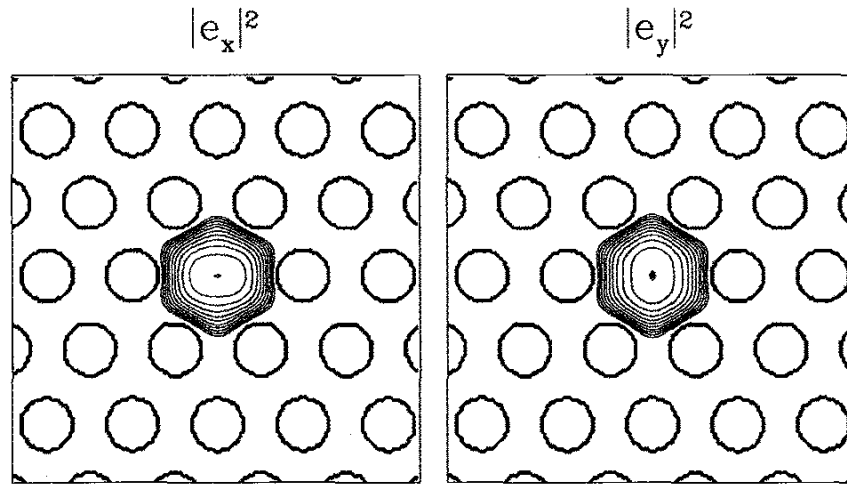


Fig. 5. Intensity in the fundamental modes at $\lambda = 1.5 \mu\text{m}$ for a HF with $d/\Lambda = 0.6$. The refractive index profile is superimposed. Left and right plots show the x - and y -components of polarization doublet, respectively. $P = 100$, $C = F = 10$. The intensity contours are spaced by 1 dB.

($d/\Lambda = 0.6$) is approximately $30 \text{ ps}\cdot\text{nm}^{-1}\cdot\text{km}^{-1}$ (i.e., anomalous dispersion) at $\lambda = 1.5 \mu\text{m}$. The way in which the GVD is calculated is described in [3].

2) *Effect of Interstitial Holes:* Section III-A1 presented the predictions for the simplest possible HF geometry. The most obvious difference between this HF and the real fiber shown in Fig. 4 is the presence of interstitial holes (see Fig. 6, which is a magnified view inside the cladding region). Indeed interstitial holes are typically present in large air fraction HF's. Here we explore the influence these additional holes have on the modal properties of the fiber. For simplicity we assume that the interstitial holes are circular, and we take the hole diameter to be d_i . Although Fig. 6 shows that they are actually somewhat triangular, this is a good approximation.

When the interstitial holes are much smaller than the wavelength of light, they do not significantly influence the fiber properties, and so the mode is hexagonal in shape (see Fig. 5). At the other extreme, when the holes are large relative to the wavelength, the modal field decays rapidly inside them, and extends out from the core between the interstitials. Hence the mode takes on the (smaller) hexagonal shape defined by this inner ring of triangular holes. Here we explore the region between these two extremes, where the effect of the interstitials on the mode properties is not so obvious. Note that when small interstitials are considered, it is crucial that P (the number of terms used to describe the cladding region) is large enough to ensure an accurate result.

When d_i (the size of the interstitials) is increased from zero the mode area decreases, as expected. For example, consider a HF with $d_i/\Lambda = 0.085$, which is approximately the diameter of circular air holes with the same area as the interstitials in the real HF shown in Fig. 4. For this d_i/Λ , we find that at $\lambda = 1.5 \mu\text{m}$ the mode area and GVD are reduced to approximately $10 \mu\text{m}^2$ and $8 \text{ ps}\cdot\text{nm}^{-1}\cdot\text{km}^{-1}$, respectively. Interestingly, we find that for this example the interstitial holes circularize the mode profile, as shown in Fig. 7. At around this value of d_i/Λ , the decrease in the intensity caused by the interstitials eliminates the filaments of light which otherwise extend between the large holes

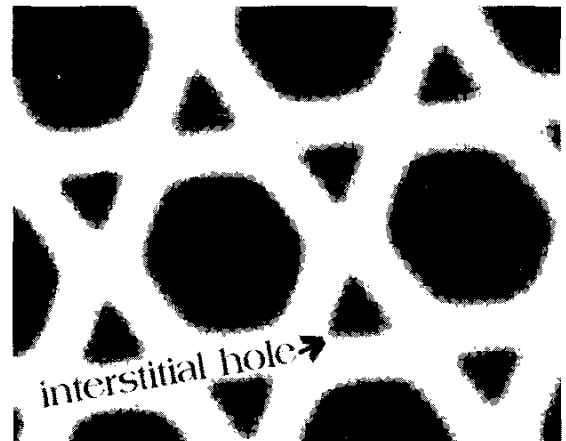


Fig. 6. Magnified view of the cladding region for the HF from Fig. 4.

(see Fig. 5). This circularization of the usually hexagonal mode shape is potentially useful, as it makes the integration of HF's with conventional fiber systems more straightforward. Indeed, even without this circularization, we have recently found that it is possible to splice HF's to conventional fiber types with a loss of only $\approx 1 \text{ dB}$ [10], which is acceptable for many device applications.

B. Mode Area of HF's

Simply altering the size or arrangement of the holes in a holey fiber can have a profound effect on its properties. One property of particular interest which can be readily tailored in HF is the area of the fundamental mode. Often a large mode area is desired so that high powers can be transmitted without inducing nonlinear effects in the fiber [11], [12]. Alternatively, small mode area fibers can be used to enhance these nonlinearities. We showed in [3] that the HF geometry offers great flexibility in the range of mode areas which can be achieved. In HF, the mode area can to a large extent be tailored via the choice of hole spacing (Λ), hole size (d/Λ), and the arrangement of these

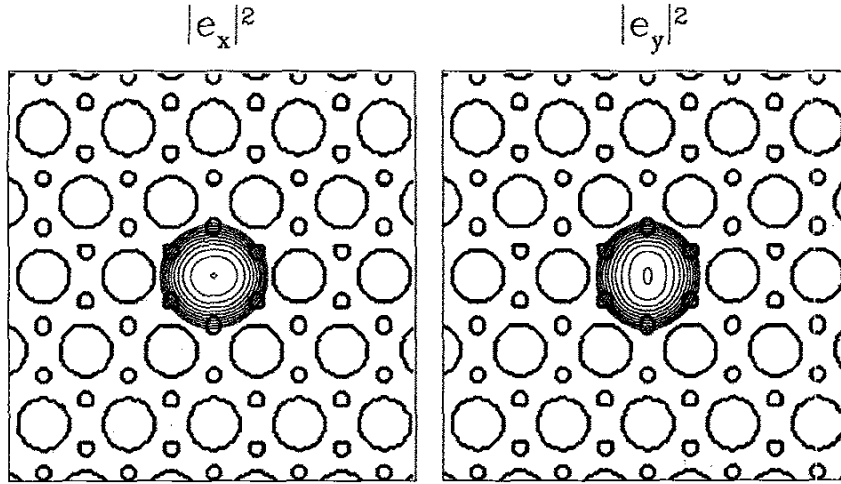


Fig. 7. Intensity at $\lambda = 1.5 \mu\text{m}$, when $d/\Lambda = 0.6$, $d_i/\Lambda = 0.085$. The refractive index profile is superimposed for $P = 300$, $C = F = 10$. The intensity contours are spaced by 1 dB.

holes. In [3], we were limited to considering fibers for which the scalar approximation is valid, and hence were restricted to HF's with small holes. Using the vector model developed in this paper, we can explore the mode areas achievable in a much fuller range of HF's.

In the small air fraction HF's considered in [3], the mode area A_{eff} (see [3]) is principally determined by the size of the core, which is defined by Λ (the separation between the holes in the HF). For such fibers, the mode size is typically a weak function of wavelength. Although shorter wavelengths decrease more rapidly inside a hole, typically very little of the modal power is located within the holes in these fibers, and so this has only a small effect on the mode size. Even with this restriction, small air fraction HF's can demonstrate a very wide range of mode areas, ranging from significantly less than one micron squared to a few hundred microns squared at $1.5 \mu\text{m}$, simply by varying Λ [3]. One disadvantage of using a large Λ to achieve a large mode area is that the bend loss of a holey fiber increases in proportion to Λ^3 [2].

We find that if Λ is smaller than the wavelength of the light guided by the fiber, then a significant fraction of the fundamental mode's power (up to $\approx 30\%$) can be located in the air holes [5]. In this regime, the mode is not as closely confined to the core, and so the mode area can be significantly larger than the core area. However, in the wavelength range of interest for telecommunications purposes, this condition is only satisfied for very small Λ , and so even though the mode size is significantly larger than the core, the resulting mode areas are still tiny. Fig. 8 shows A_{eff} for a range of such HF's; note that the results for the x and y -components of the polarization doublet which forms the fundamental mode are very similar. These fibers have very small mode areas, on the order of a micron squared. One potential application of such fibers is in exploring nonlinear effects, as the tight mode confinement implies that such effects should be present even at quite moderate powers.

Simply by increasing the distance between the holes A_{eff} can be increased dramatically. This is demonstrated in Fig. 9, which gives results for a spacing of $\Lambda = 23 \mu\text{m}$. This was chosen

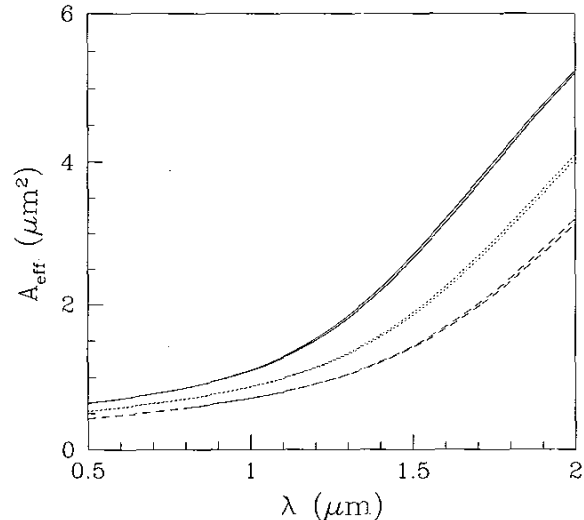


Fig. 8. $A_{\text{eff}}(\lambda)$ for a range of HF's with large holes. $\Lambda = 0.75 \mu\text{m}$, the solid, dotted and dashed pairs of lines correspond to $d/\Lambda = 0.7, 0.8$, and 0.9 , respectively, each pair is comprised of the result for the x and y -components.

to correspond to the HF described in [13], which indicates that it is feasible to fabricate such HF's. This graph indicates that rather large mode areas of the order of a few hundred squared microns are possible in these fibers. Figs. 8 and 9 both suggest that regardless of Λ , A_{eff} is larger when the air fill fraction is lower. This occurs because when the holes are small, the degree to which the modal field decays within them is also small, and so the field extends further into the cladding region.

IV. DISCUSSION AND CONCLUSION

The full vector model developed in this paper is a powerful predictive tool which allows us to calculate the modal properties of a much fuller range of holey fibers than previous scalar techniques. It is an efficient and accurate alternative to existing techniques. Recently this model was validated against experiment by comparing the predictions for the group velocity dis-

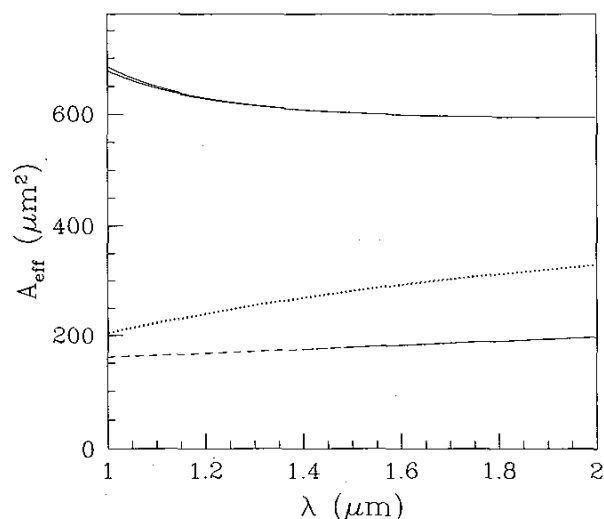


Fig. 9. $A_{\text{eff}}(\lambda)$ for a range of HF's with $\Lambda = 23 \mu\text{m}$. The solid, dotted and dashed pairs of lines correspond to $d/\Lambda = 0.5, 0.7,$ and $0.9,$ respectively, each pair is comprised of the result for the x - and y -components.

persion with measured values for a particular HF [10]. This is a stringent test, and allows us to have confidence in the predictions made by our model.

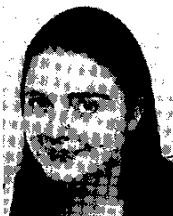
In Section III-A2, predictions were made for one HF which we have fabricated. We find that it is possible to produce HF which has a circular fundamental mode rather than the more typical hexagonal shape. This is an advantage because it allows for more straightforward integration with conventional fiber systems.

Both here and in [3], we have shown that the complicated cladding structure of HF leads to highly unusual and tailorable modal properties. For example, in Section III-B, we showed that the mode area in HF's can be tailored over three orders of magnitude. This high degree of flexibility means that HF's can be designed to suit a very wide range of applications. Using the new efficient vector model developed here, many other properties of large air fraction holey fibers can now be explored. For example, the extremely large index difference between the core and cladding in HF's can lead to very high dispersion in these fibers. Using the new model developed here, it is now possible to explore the range of HF's which may be suited to dispersion compensation applications.

REFERENCES

- [1] T. A. Birks, P. J. Roberts, P. St. J. Russell, D. M. Atkin, and T. J. Shepherd, "Full 2-D photonic bandgaps in silica/air structures," *Electron. Lett.*, vol. 31, pp. 1941–1942, 1997.
- [2] T. A. Birks, J. C. Knight, and P. St. J. Russell, "Endlessly single-mode photonic crystal fiber," *Opt. Lett.*, vol. 22, pp. 961–963, 1997.
- [3] T. M. Monro, D. J. Richardson, N. G. R. Broderick, and P. J. Bennett, "Holey optical fibers: An efficient modal model," *J. Lightwave Technol.*, vol. 17, pp. 1093–1102, 1999.
- [4] T. M. Monro, D. J. Richardson, and P. J. Bennett, "Holey optical fibers: An efficient modal model," in *Proc. OFC'99*, 1999, paper FG3.
- [5] —, "Holey fibers for evanescent field devices," in *Proc. CLEO'99*, 1999, paper CTuK70.
- [6] T. M. Monro, D. J. Richardson, and P. J. Bennett, "Developing holey fibers for evanescent field devices," *Electron. Lett.*, vol. 35, pp. 1188–1189, 1999.

- [7] A. Ferrando, E. Silvestre, J. J. Miret, P. Andres, and M. V. Andrés, "Full-vector analysis of a realistic photonic crystal fiber," *Opt. Lett.*, vol. 24, pp. 276–278, 1999.
- [8] D. Mogilevtsev, T. A. Birks, and P. St. J. Russell, "Group-velocity dispersion in photonic crystal fibers," *Opt. Lett.*, vol. 23, pp. 1662–1664, 1998.
- [9] A. Snyder and J. Love, *Optical Waveguide Theory*. London, U.K.: Chapman and Hall, 1995.
- [10] P. J. Bennett, T. M. Monro, and D. J. Richardson, "Toward practical holey fiber technology: fabrication, splicing and characterization," presented at the Proc. ECOC'99, 1999.
- [11] Y. Liu and G. Berkey, "Single-mode dispersion-shifted fibers with effective area over $100 \mu\text{m}^2$," in *Proc. ECOC'98*, 1998, pp. 41–42.
- [12] H. L. Offerhaus, N. G. Broderick, D. J. Richardson, R. Sammut, J. Caplen, and L. Dong, "High-energy single-transverse-mode Q -switched fiber laser based on a multimode large-mode-area erbium-doped fiber," *Opt. Lett.*, vol. 23, pp. 1683–1685, 1998.
- [13] J. C. Knight, T. A. Birks, R. F. Cregan, P. St. J. Russell, and J. P. de Sandro, "Large mode area photonic crystal fiber," *Electron. Lett.*, vol. 34, pp. 1347–1348, 1998.



Tanya M. Monro received the Ph.D. degree in self-written waveguides from Sydney University, Sydney, Australia.

She is currently a Research Fellow at the Optoelectronics Research Centre (ORC), Southampton University, U.K., working in the area of modeling and characterizing holey optical fibers.

Dr. Monro was awarded the 1998 Bragg Gold Medal for the best physics Ph.D. dissertation in Australia.



D. J. Richardson currently holds a Royal Society Research Fellowship, and is a Group Leader at the Optoelectronics Research Centre (ORC), Southampton University, U.K. His current research activities include advanced communications, high-power fiber lasers, ultrafast lasers, and the applications and physics of microstructured nonlinear/linear media.



N. G. R. Broderick received the Ph.D. degree in gap solitons from Sydney University, Sydney, Australia.

He is currently a Research Fellow at the Optoelectronics Research Centre (ORC), Southampton University, U.K.



P. J. Bennett received the Ph.D. degree in physics and astronomy from Southampton University, Southampton, U.K., in 1998.

He is now working on the fabrication of holey fibers at the Optoelectronics Research Centre (ORC), Southampton University.